Stardust-NExT NAVCAM Calibration and Performance

(9/01/11 preprint version)

Kenneth P. Klaasen,[1*] David Brown,[1] Brian Carcich,[2] Tony Farnham,[3] William Owen,[1] Peter Thomas[2]

[1]Jet Propulsion Laboratory, California Institute of Technology, Mail Stop 306-392, 4800 Oak Grove Dr., Pasadena, CA 91109, USA
[2]Cornell University, Space Sciences Building, Ithaca, NY 14853, USA
[3]Department of Astronomy, University of Maryland, College Park, MD 20742-2421, USA

*to whom all correspondence should be addressed: email kenneth.p.klaasen@jpl.nasa.gov, phone 818-354-4207, fax 818-393-3290

Abstract

NASA's Stardust-NExT mission used the Stardust spacecraft to deliver a scientific payload, including a panchromatic visible camera designated NAVCAM, to a close flyby of comet 9P/Tempel 1 in February 2011. Proper interpretation of the NAVCAM images depends on accurate calibration of the camera performance. While the NAVCAM had been calibrated during the primary Stardust mission to comet 81P/Wild 2 in 2004, that calibration was incomplete and somewhat lacking in fidelity. Substantial improvements in the NAVCAM calibration were achieved during Stardust-NExT in the areas of geometric correction, spatial resolution, and radiometric calibration (in particular, zero-exposure signal levels, shutter time offsets, absolute radiometric response rate, noise characterization, and scattered light problems). This improved calibration will allow upgrades to the calibration of images returned from the Stardust primary mission as well as high-quality calibration of the Stardust-NExT images. The upgraded calibration results have been incorporated into the Stardust-NExT image processing pipeline via new routines and updated constants and files in preparation for archiving calibrated images in the NASA Planetary Data System.

Keywords: Comet Tempel 1, instrumentation, data reduction techniques

1. Introduction

NASA's Stardust-NExT spacecraft carried a payload of three scientific instruments during its extended mission to encounter comet 9P/Tempel 1 in February 2011 – a visible camera dubbed NAVCAM, and two dust detection instruments. This spacecraft and instrument suite were also used previously on the Stardust primary mission to comet 91P/Wild 2 in January 2004. The NAVCAM was included in the Stardust payload primarily as a navigation tool to facilitate optical navigation to the desired flyby points at asteroid Annefrank and comet Wild 2 and autonomous tracking of the target bodies during the flybys. The NAVCAM's role as a scientific imager was secondary. Therefore, while NAVCAM fulfilled its duties admirably during the primary mission (Duxbury, et al., 2004; Tsou, et al., 2004; Brownlee, et al., 2004), and a set of wonderful images of Wild 2 was transmitted to Earth, limited resources and effort were expended during the Stardust mission on achieving high-precision characterization of the NAVCAM performance for scientific calibration of those images (Newburn, 2000).

NASA approved a proposal to use the still healthy Stardust spacecraft to perform an extended mission to Tempel 1 – called Stardust New Exploration of Tempel 1, or Stardust-NExT (Veverka, et al., 2011a). For this new mission, the science priorities changed, and the NAVCAM images became the highest priority science measurements. Therefore, it was appropriate to expend substantial effort to improve and extend the inflight calibration of the NAVCAM during Stardust-NExT. This paper documents the improvements, corrections, and extensions of the NAVCAM calibration.

First we provide a brief description of the NAVCAM instrument and summarize the calibration data collected during the Stardust-NExT mission. NAVCAM calibration results are then discussed with emphasis on the differences from the previously reported calibrations. The calibration is addressed in the areas of geometric measurement accuracy, spatial resolution achieved, and radiometric measurement accuracy. Finally, the data calibration processing pipeline is described along with the plans for data archiving in the NASA Planetary Data System (PDS).

2. NAVCAM Description

The NAVCAM was constructed using a number of spare subassemblies left over from previous flight projects. The optics are spare Voyager Wide-Angle Camera optics with a 200-mm focal length operating at f/3.5. The detector is a spare Cassini 1024x1024-pixel CCD; coupled with the optics, it provides a field of view (FOV) of about 3.5° (60 μrad/pixel). We adopt a convention in which pixel coordinate locations within the FOV are designated by line and sample values; lines increment in the vertical direction, i.e., the direction of CCD parallel charge transfer along columns, and samples increment in the CCD horizontal direction, i.e., the direction of CCD serial register readout. NAVCAM includes spare Voyager shutter and filter-wheel mechanisms. The filter wheel in the camera failed early in the primary mission, so all subsequent images were acquired through the broadband optical-navigation spectral filter (475 –

925 nm). NAVCAM includes an internal calibration lamp that serves as a test source to check camera aliveness, but the illumination on the detector is not uniform, so the cal lamp's utility as a flat-field calibration source is limited. Image data can be returned either fully encoded to 12 bits or compressed to 8 bits per pixel using an onboard lookup table. Images can be edited onboard to return only one or more specified window areas from the frame. The spacecraft data system can support a maximum imaging rate of one full frame every 6s for compressed data. The camera boresight is pointed using a combination of spacecraft attitude and a one-axis scan mirror that sweeps the boresight through 180° in a half-plane centered in the direction opposite the solar panel normal and containing the spacecraft dust shield direction (0° mirror angle). At mirror scan angles below 16°, the view is through a periscope used to protect the optics from dust damage during the comet flyby. Figure 1 shows a picture of the NAVCAM and its scan mirror. A complete description of the NAVCAM is provided in Newburn, et al., (2003a).

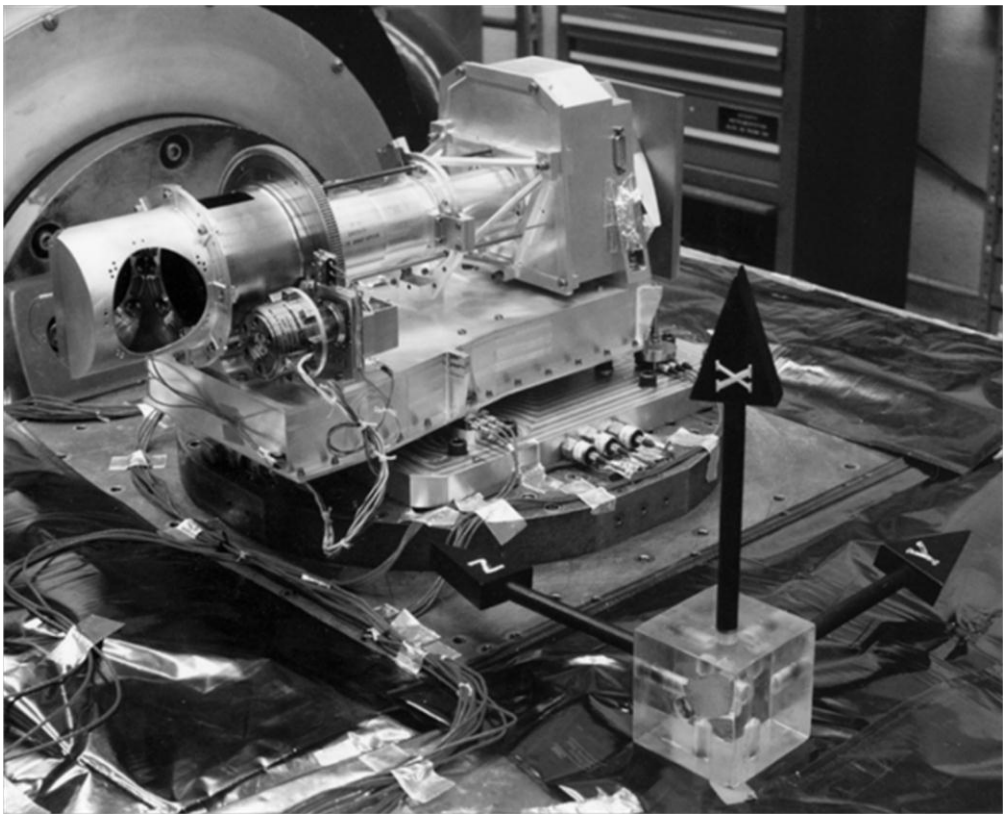

Figure 1 – The Stardust-NExT NAVCAM including its scan mirror mechanism on a laboratory bench prior to launch

The NAVCAM suffers from a number of problems that ordinarily are not encountered in other high-quality scientific spaceflight cameras (probably due to the lack of science priority on the NAVCAM for the primary mission). First, early in the prime mission contamination was observed to have accumulated within the NAVCAM that resulted in severe blurring of the images (Hillier, et al., 2011; Newburn, et al., 2003a & b; Tsou, et al., 2004; Li, et al., 2009).

This contamination appears to get deposited on the CCD window (either inside the package or outside) when the CCD is cold. Heating the CCD was found to remove the contamination (mostly) and to allow good image quality, but eventually the contamination gets redeposited. The contamination was successfully controlled by periodic heating of the instrument using its internal electrical heaters and by placing direct sunlight on the camera radiator (called "bake" maneuvers). Second, the CCD temperature is not controlled, and drifts in temperature cause changes in the calibration. Third, no pre-exposure flush of accumulated CCD dark charge is executed automatically; therefore, dark current builds up during the entire (variable) period between successive CCD readouts. Fourth, the NAVCAM images exhibit horizontal bars of coherent noise across most of the array whose source is unknown and that increase the background noise from about 1 DN (data number) to 3 – 4 DN. And last, experience has shown that scattered light rather easily enters the system, especially at high and low scan mirror angles.

3. Inflight Calibration Data

The performance of the NAVCAM was monitored throughout the Stardust-NExT extended mission using a standard calibration sequence along with a few special calibrations. Calibrations involved imaging of a variety of stars, several of which are photometric standards, acquiring dark frames, and taking images illuminated by the NAVCAM internal calibration lamp. The cruise calibrations allowed characterization of camera imaging performance in the areas of geometric fidelity, spatial resolution, and radiometry (including zero-exposure signals, shutter times, linearity, field flatness, noise, and radiometric response rate) more accurately than had been possible during the primary mission. Preliminary radiometric calibration results have been incorporated into the image processing pipeline. Special observations, including new analysis of some of the Stardust prime mission data, allowed determination of the NAVCAM periscope throughput as a function of scan mirror angle, scattered light levels from the spacecraft structure as functions of mirror angle and the Sun illumination direction on the spacecraft, and charge bleeding and residual image in the CCD detector. Calibration sequences similar to the standard cruise calibration were also executed at Encounter (E) -18 days and at E+10 days. Table 1 summarizes the data taken during the Stardust-NExT mission that are useful for NAVCAM calibration.

Selected data from the prime mission were also analyzed to broaden and deepen our understanding of the NAVCAM performance in areas where the NExT data are not sufficient in themselves. The prime mission data span a larger range of CCD temperatures, heater-off times, power-on times, scan mirror angles, and S/C attitudes with respect to the Sun than did the NExT mission alone. Almost all of the prime mission images are useful for camera calibration in one way or another. Table 2 summarizes the NAVCAM performance aspects that were more fully addressed using prime mission data and the general types of data used.

Date of Acquisition	Activity	Data type	Target	Purpose	Comments
1/25/2007	Periscope test	0° mirror angle and cal lamp images	Dark sky, cal lamp	Check camera and periscope health	Cal lamp image failed due to command queue error
1/31/2007	Star imaging	Star and cal lamp images	Star, cal lamp	Check camera contamination level	Cal lamp image failed due to command queue error
10/12/2007	Pre-bake characterization	Star and cal lamp images	Antares, cal lamp	Determine contamination state and troubleshoot cal lamp problem	One of two cal lamp images failed due to command queue problem
10/25/2007	Post-bake characterization	Star images and dark frame	Antares	Verify removal of contamination	Camera clean, useful psf data
1/25/2008	Cal lamp test	Windowed cal lamp frames	Cal lamp	Verify proper commanding of cal lamp frames	Successful
12/3/2008	Pre-bake characterization	Star, dark, and cal lamp images	Elnath	Determine contamination state	Camera contaminated
12/15/2008	Post-bake characterization	Star, dark, and cal lamp images	Dubhe	Verify removal of contamination	Camera clean, useful psf data
12/20/2008	Standard cruise cal	Star, dark, and cal lamp images	Canopus, bet Hyi, Achernar, Vega, 16CygA	Radiometry, psf, shutter offset, scattered light at encounter attitude, flat field	Good data set
12/31/2008	Contamination check	Star, dark, and cal lamp images	Procyon	Verify camera remains clean for upcoming Moon imaging	Camera clean, useful psf data
1/12/2009	Periscope test	Moon and dark images	Moon	Determine image quality and throughput of periscope vs. mirror angle	Good data set
1/12/2009	Contamination check	Star, dark, and cal lamp images	β Per	Verify camera remained clean for prior Moon imaging	Camera clean, useful psf data
8/6-8/2010	Pre-bake characterization	Star, dark, and cal lamp images	Regulus	Characterize elevated fixed-pattern noise (FPN) with extended camera power on time and its dependence on contamination level	Camera contaminated, elevated FPN seen after 16 hr of power on in shuttered frames only
8/11-13/2010	Post-bake characterization	Star, dark, and cal lamp images	Regulus	Characterize elevated fixed-pattern noise with extended camera power-on time and its dependence on contamination level	Camera clean, elevated FPN seen after 16 h of power on in shuttered frames only; useful psf data
8/23/2010	Unpointed portion of standard cruise cal	Cal lamp and dark images	Cal lamp	Dark signal, shutter offset, flat field	Good data set
1/27/2011	Standard cruise cal (pre-encounter)	Star, dark, and cal lamp images	Canopus, bet Hyi, Achernar, Vega, 16CygA	Radiometry, psf, shutter offset, data compression	Good data set
2/25/2011	Standard cruise cal (post-encounter)	Star, dark, and cal lamp images	Canopus, bet Hyi, Achernar, Vega, 16CygA	Radiometry, psf, shutter offset, data compression, flat field	Good data set

Table 1 – Summary of NAVCAM calibration data taken during the Stardust-NExT mission

NAVCAM performance characteristic analyzed	Stardust prime mission data used
Bias and dark current levels	Zero-exposure full frames and full frames of stars with mostly dark sky
Shutter polarity determination	Early cruise frames (n0112-113), Moon images (n0198-219), Annefrank images (n0371-476), Wild 2 images (n2052-2113)
Periscope throughput	Spica (n0247-49 & n0254-55), Pleiades (n0477-507), Wild 2 (n2005-63)
Extended power-on fixed pattern noise	Wild 2 approach (n0528-1023)
Scattered light	Opnav-filter star images (preferably full frames) at a variety of mirror angles and S/C attitudes including: n0165-308, selected Annefrank images, n0477-529, selected windowed frames from Wild 2 approach at different mirror angles, n0634-48, n0869-76, most Wild 2 encounter frames, n02125, n02127

Table 2 - NAVCAM calibration data from the Stardust prime mission that were used to extend the characterization of camera performance

4. Geometric Calibration

Focal length and geometric distortion

The focal length and geometric distortion of the NAVCAM were determined using images of the Pleiades star field. The usual technique is to relate the observed coordinate of each star image on the detector (x_p, y_p in mm from the optical center derived from sample/line coordinates at 0.012 mm/pixel) to an "undistorted" position as

x_p=(sample-oc_x)/pixel
y_p=(line-oc_y)/pixel

R=sqrt(x_p^2+y_p^2)= radius from optical center
x_c=x_p * (1 + k*R^2)
y_c=y_p * (1 + k*R^2)

where oc_x and oc_y are the optical center coordinates in pixels,
pixel = 83.3333 pixel/mm,
x_c, y_c are the undistorted positions (mm), and

k is the "distortion coefficient."

The differences between observed and predicted positions on the detector are the residuals, and the solution is taken where the sum of squares of the residuals is minimized. The optical center was only weakly defined, so it was assumed to be at (512.5, 512.5).

Stellar image positions are located by a centroiding algorithm, and their RA, Dec locations (Hog, et al., 2000) and image locations in pixels are recorded. The Pleiades image contained 99 stars bright enough to be accurately centroided. The solution of predicted versus actual positions on the detector includes camera orientation, focal length (fl), and distortion (k). The solution gave a focal length = 201.136 ± 0.01 mm and k = 5.24×10^{-5} mm^{-2}. These are small distortions. Residuals were ~0.1 pixel.

Spatial resolution

The NAVCAM point-spread function (psf), defined as the fraction of the total point-source signal captured in a given pixel as a function of the pixel's distance from the center of the psf, was determined from star images having minimal smear and obtained with an uncontaminated camera. The best psf solution to apply to the Tempel 1 encounter images is one based on the images of Canopus taken during the pre- and post-encounter calibrations. These images exposed Canopus to a peak signal of approximately ½ full scale, 10x that level, and 100x that level to allow determination of the psf core along with the wings. These images yielded good quality psf measurements out to about 15 pixels from the centroid. An image of Procyon taken in December 2008 with a peak signal of about 500x full scale was used to extend the psf determination out to 70 pixels from the centroid – a signal level of about 10^{-6} of the total star signal.

The data indicate that the psf is radially symmetric to within the accuracy of the measurements. No measureable differences in the psf were observed during the NExT mission when the camera was uncontaminated. Figure 2 shows the psf data along with piecewise functional fits to the data; both semi-log and log-log plots are presented.

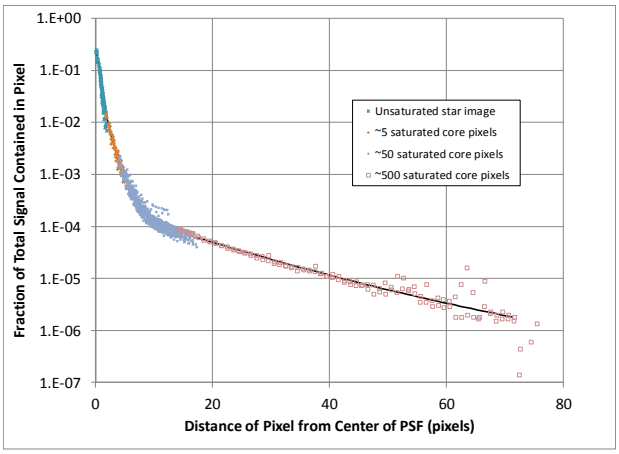

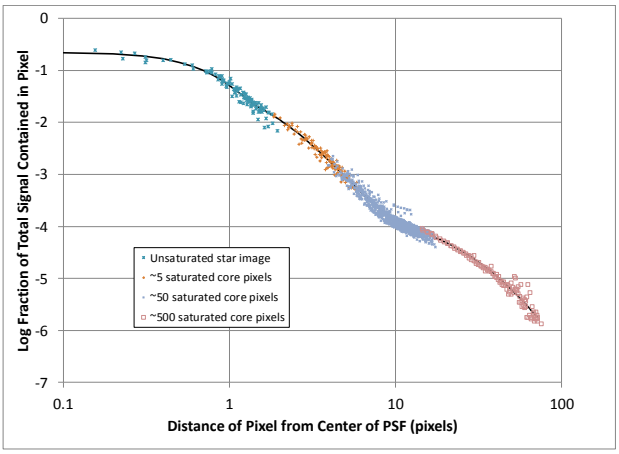

Figure 2 - NAVCAM psf vs. distance data and piecewise functional fits on linear and log scales

The psf piecewise functional fits are:

Distance from psf centroid (pixels)	psf function
0 to 1.4046	$psf = 10^{-0.0193x^6 + 0.184x^4 - 0.7983x^2 - 0.6557}$
1.4046 to 5. 65	$psf = 10^{3.06E-02x^2-0.5818x-0.9058}$
5. 65 to 17.307	$psf = 10^{1.658E-05x^4-1.882E-03x^3+5.822E-02x^2-0.7402x-0.57}$
17.307 to 75	$psf = 10^{1.1662E-04x^2 - 3.8699E-02x - 3.5758}$

These functions can be used as a spatial resolution enhancement filter if so desired for images taken with the optical-navigation filter.

The fraction of total point source signal in the central pixel can range from 0.22 if the psf is perfectly centered down to 0.07 if the centroid is located at the corner of a pixel. The psf full width at half maximum (FWHM) is 1.29 pixels. No degradation in the psf has been observed due to buildup of residual instrument contamination.

5. Radiometric Calibration

Response linearity and shutter time offsets

CCD detectors of the type used in NAVCAM are inherently linear in their response with respect to incident photon flux. The linearity of the NAVCAM detector was confirmed by pre-launch calibrations (Newburn, 2000). Response linearity was verified in flight using cal lamp images. The NAVCAM response in sets of cal lamp images with increasing exposure times can be modeled extremely well by a perfectly linear detector response coupled with fixed line-dependent shutter time offsets (i.e., actual – commanded exposure times). Such models fit the observed data to better than 0.1%.

The NAVCAM shutter blades move across image lines when making an exposure. The blades move in alternating directions in successive frames (designated "forward" and "reverse"). The blades always move in the "forward" direction after a NAVCAM power cycle. The shutter blade movement polarity is not reset by a commanded dark frame.

The exposure time offsets are different for "forward" and "reverse" motion. On average, exposures are ~0.4 ms longer than commanded for "forward" motion and ~1.4 ms shorter than commanded for "reverse" motion. However, there is variation in the offset at each image line in both cases. It was not possible to calibrate the shutter offset at each image line in flight due to downlinked data volume limitations. Therefore, we refer back to shutter offset curves derived from ground-based calibrations to estimate how the offsets vary with line number. Offset curves

were derived from integrating sphere flat-field images taken over a range of exposure times and at different CCD temperatures. These curves are shown in Figure 3 along with the offsets derived at three specific image lines from inflight cal lamp frames taken with short exposure times (ranging from 0 to 35 ms). Note that the ground-based offsets taken at a CCD temperature of -30°C have similar line dependence to the flight data (which makes sense, since that temperature is closest to the -24°C temperature that applied when the flight data were taken). Therefore, the inflight shutter offset line dependence was estimated by scaling the -30°C ground-based offsets to fit the inflight results at three points using a quadratic scaling function.

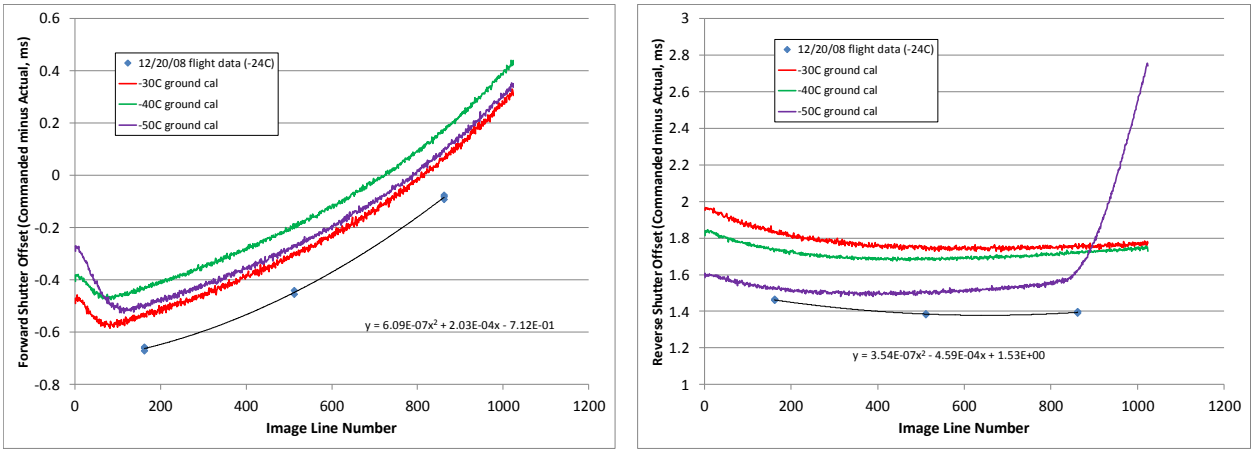

Figure 3 - Line-dependent shutter time offsets derived from ground-based and inflight calibrations (left – "forward" blade motion; right – "reverse")

Shutter offset calibration data were taken four times during the NExT mission at four slightly different CCD temperatures. The resulting data and the scaled line-dependent fits are shown in Figure 4. The offsets derived from the August 2010 calibration were selected for application to the Tempel 1 encounter data, since the CCD temperatures matched best. Note that to compute the correct shutter polarity for any given frame, a supplemental command history file is required to determine when all NAVCAM power off/on commands, all imaging commands for non-returned frames, and all dark-frame image commands were issued, since this information is not available in the raw image headers. The polarity information is then inserted into the calibrated frame headers.

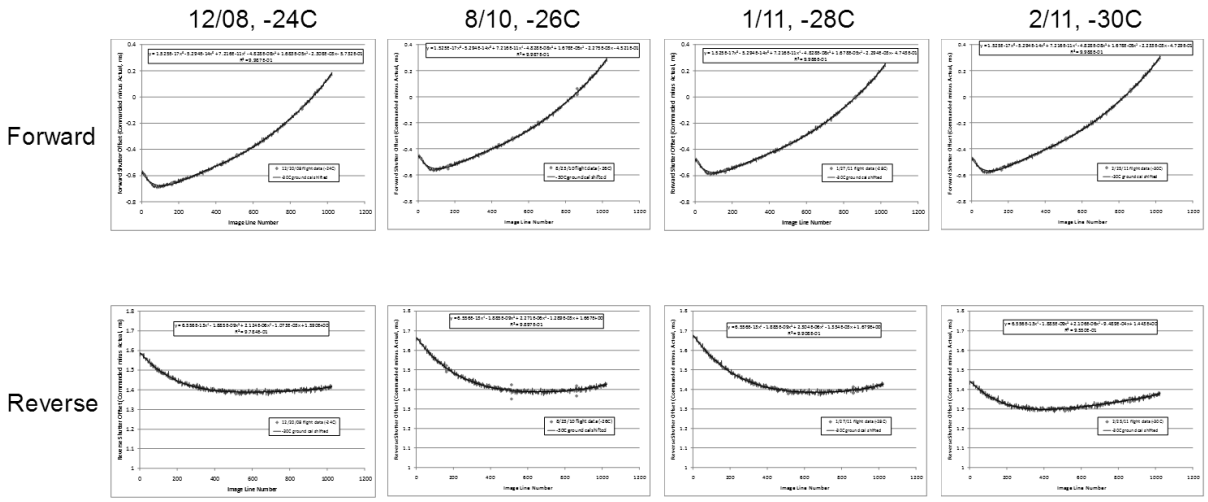

Figure 4 - NAVCAM shutter time offsets vs. line number for blade motion in both directions derived from four different calibrations during NExT

Noise

NAVCAM data include four types of noise – detector read noise, photon shot noise, coherent noise, and fixed-pattern noise. Read noise has been measured in differenced dark frame pairs to be ~1.35 DN (1σ, uncompressed). This level applies outside the horizontal coherent noise bars. Within the coherent noise bars, the random noise level is increased to ~4.1 DN uncompressed (this level of noise is barely detectable in compressed frames). The coherent noise bars are ~17 lines high and repeat every ~29 lines (~10 Hz cycle) and are shown in Figure 5. The mean DN level within the bars is unchanged from that outside the bars. The cause of the coherent noise is unknown. Attempts to remove the coherence leave residual random noise at the ~3.1 DN level. No attempt to remove coherent noise was included in the image processing pipeline.

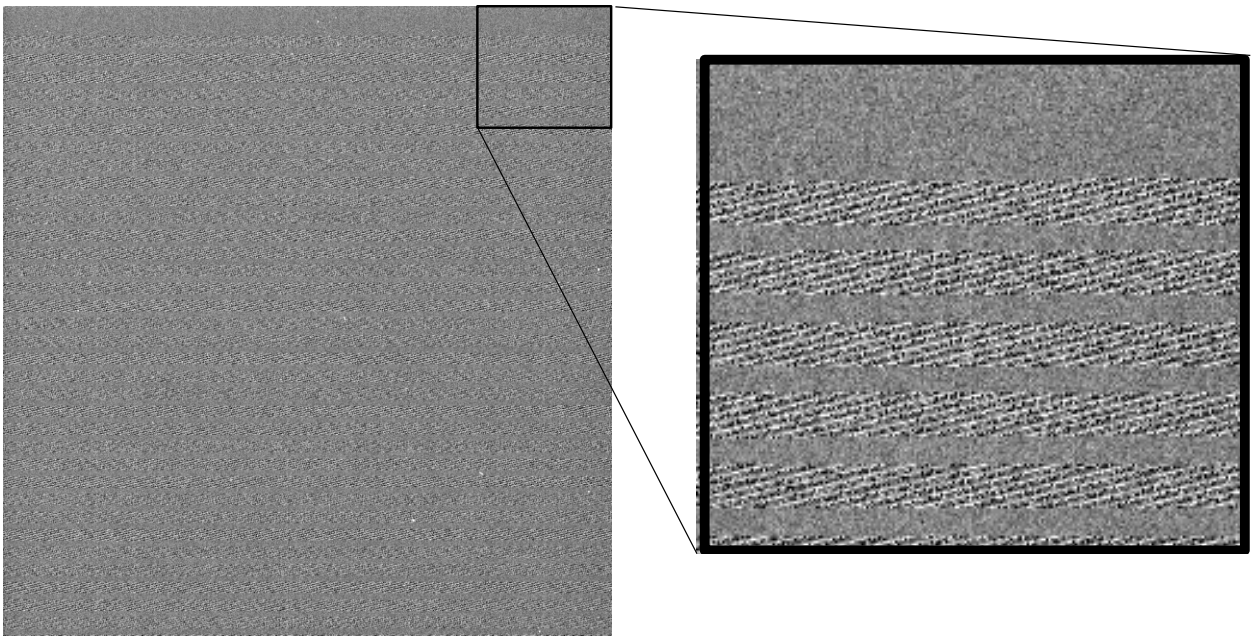

Figure 5 - NAVCAM dark frame contrast enhanced to show coherent noise bars

The NAVCAM detector exhibits fixed-pattern noise (FPN) in certain circumstances. This type of noise was first observed on the approach to Wild 2 in the prime mission when the camera was left powered on for an extended period in excess of two weeks (normally the camera had been powered on only long enough to capture a small data set – usually a few minutes, perhaps up to 2 hours maximum). The Wild 2 approach data suggested that the FPN arises after the NAVCAM has been powered on for >10 hr. The rise in FPN is accompanied by an associated rise in CCD temperature. It occurs independent of the contamination level of the camera. But a peculiar aspect of the FPN is that even after long power-on times with elevated CCD temperatures, the FPN does not show up in dark frames, only in those that have had the shutter open to admit some level of external photons (even if only a low-level scattered light background).

Further investigation of the FPN during NExT showed that the FPN level also depends on the amount of background scattered light in an image. The Wild 2 approach images had scattered light levels of <100 DN and raw FPN amplitudes of 6 – 20 DN rms. But during the NExT approach to Tempel 1, much higher levels of scattered light were encountered, and the FPN amplitude increased to 25 - 45 DN rms even when the camera had been powered on for only a short time and the CCD temperature remained low.

These observations lead us to speculate that the FPN has two sources – hot pixels that generate dark current at higher than typical rates, which are exaggerated by warm CCD temperatures, and enhanced-response pixels that are more sensitive to incident photons than typical pixels. Oddly, incident light appears to be needed to trigger both types of FPN pixels; even the hot pixels do not produce excess charge unless the shutter is opened. In this FPN model, hot pixels dominate at

low scattered light levels (but require elevated CCD temperatures) while enhanced-response pixels dominate at high scattered light levels. Figure 6 illustrates the FPN dependence on scattered light level and camera power-on time. Since FPN was not seen in any pre-launch integrating sphere images, we expect that both types of FPN pixels are a result of radiation damage to the CCD accumulating in flight.

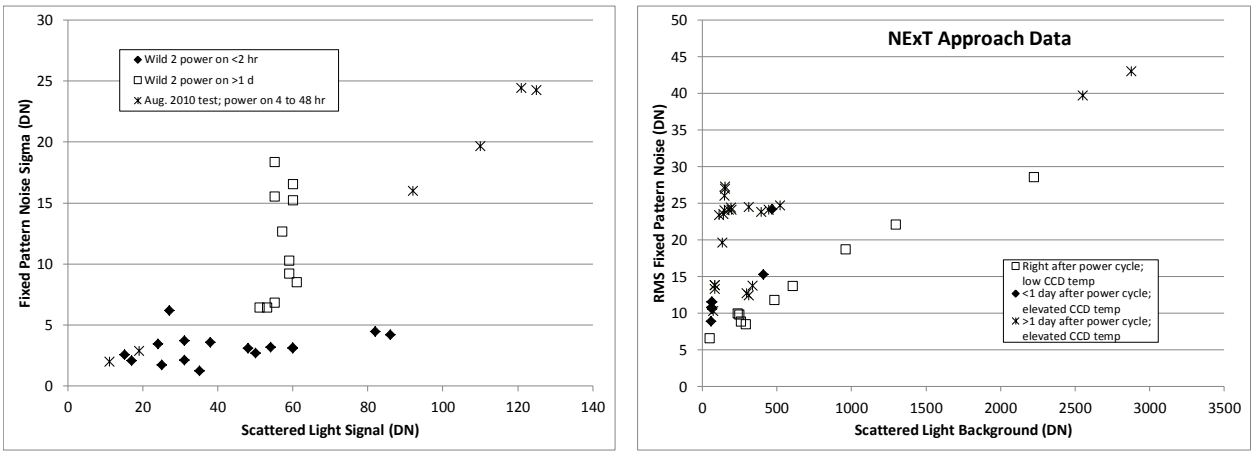

Figure 6 - NAVCAM fixed pattern noise dependence on background scattered light level and camera power-on time

The hypothesis that some of the FPN source pixels are hot pixels that generate excessive dark current was investigated by looking at the behavior of a few individual pixels. Their signal generation rates were calculated over a range of CCD temperatures. As shown in Figure 7, the dependence of the signal generation rates of these pixels on CCD temperature is very typical of that of thermal dark current. However, the signal levels in these pixels at a given CCD temperature are proportional to image integration time (i.e., the length of time the shutter is open), not to the time between CCD reads. This observation provides more evidence that these hot pixels need incident light to trigger them. We do not understand the device physics that requires incident photons to produce enhanced thermal dark current rates in selected pixels, but that seems to be what is happening.

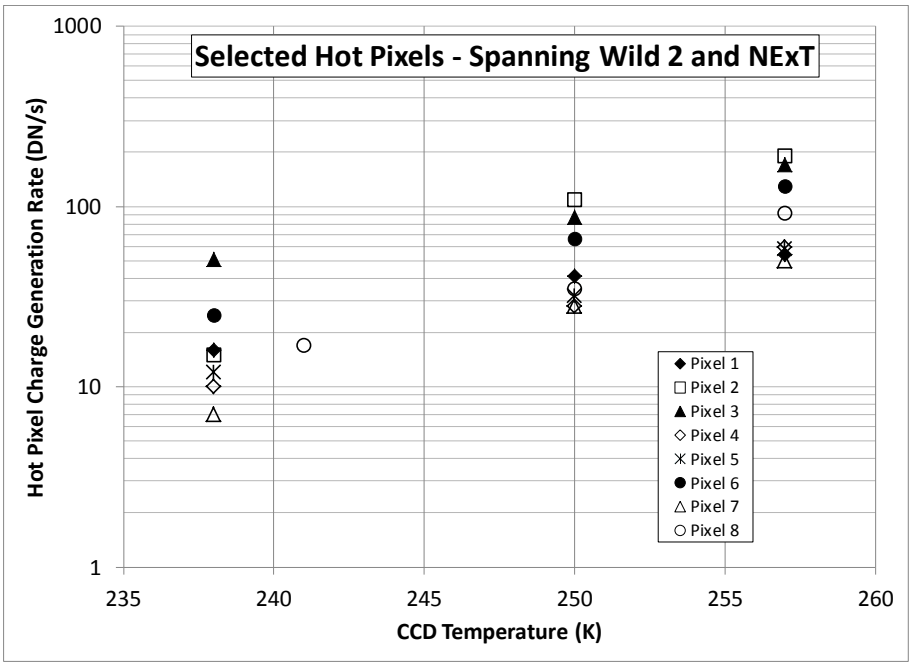

Figure 7 - Hot-pixel charge generation rates vs. CCD temperature are typical of thermally generated charge

The FPN can be largely eliminated by successive frame differencing when identical frame pairs are acquired. No evidence of FPN is found in the Tempel 1 close encounter images, which were acquired using data compression, at short power-on time, and with minimal scattered light. No attempts to correct for FPN are included in the NAVCAM processing pipeline.

Gain and full well

Photon shot noise allows a determination of the NAVCAM system gain constant (e^-/DN) using the photon transfer technique (i.e., plotting random noise vs. signal from differenced cal lamp images and dark frames; Janesick, et al., 1987). Figure 8 gives an example photon transfer curve illustrating the derivation of gain and read noise. The read noise represents an average across the frame including both coherent noise areas and areas free of coherent noise. The gain constant has gradually increased during the NExT mission from about 25 e^-/DN in December 2008 to about 27.5 e^-/DN in February 2011. However, the gain constant is not used explicitly in radiometric calibration; it is subsumed in the absolute radiometric conversion factor (converting from DN to scene radiance). Note that ADC saturation (4095 DN) is reached before CCD full well.

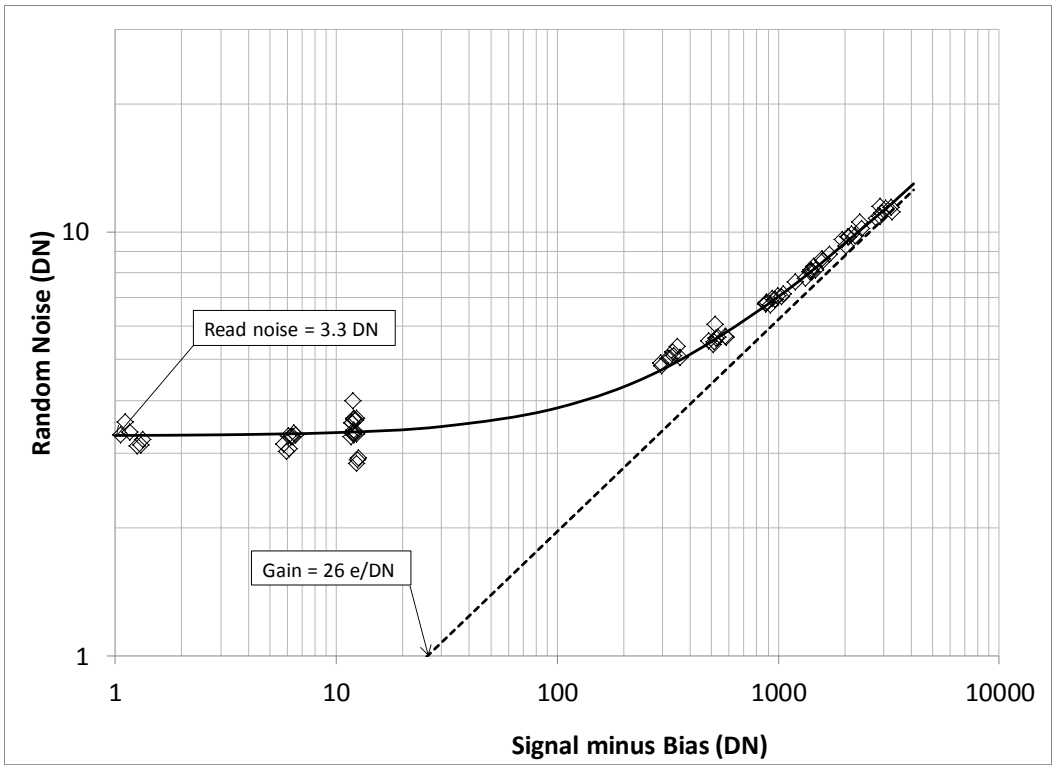

Figure 8 - NAVCAM photon transfer curve determination of the system gain constant (e^-/DN)

Zero-exposure signal level

Knowledge of the zero-exposure bias level and dark current buildup are essential to proper radiometric image calibration. The bias level can be determined from the serial overclocked pixels (Newburn, et al., 2003a). However, the serial overclocked pixels do not all accurately reflect the bias level within the active area of the detector array. Figure 9 shows the difference between the mean DN value in the active area of a dark frame and the leading and trailing overclocked pixel values. The overclocked pixel values from columns 1044 – 1046 are the closest to the mean value in the active array; therefore, we use these columns to derive the bias level in the calibration pipeline.

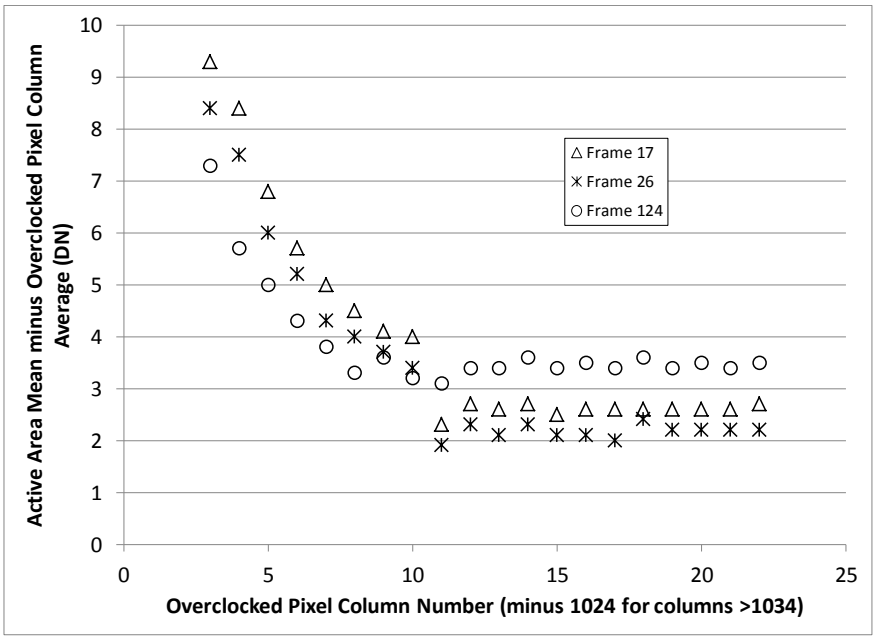

Figure 9 - Difference between dark-frame mean DN and serial overclocked pixel values for the available overclocked pixel columns

However, no overclocked pixels are returned for windowed images, and a large number of windowed images were taken during NExT. So another approach is required to estimate the correct bias for windowed frames. Analysis of the overclocked pixel bias levels from frames acquired at a variety of CCD temperatures during both Stardust and NExT shows that the bias varies with CCD temperature at a rate of ~3.5 DN decrease for every 1°C increase in CCD temperature. But other factors also affect the bias. The bias level seems to be correlated with the time since the CCD heater was last on (which may be a proxy for the level of contamination, but why the contamination level should affect the bias is unknown). No other correlations have been found. Figure 10 illustrates the dependence of the bias level on time since the CCD heater was turned off and on the CCD temperature. We model the bias dependence on heater-off time by

> Bias (DN at CCD temp of 240.795°C) = 20.435 ln (heater-off time in days if between 0.1 and 100 days, else 0.1 or 100 days) + 427.53

and then adjust for differing CCD temperature using the -3.5 DN/degree factor. The residual uncertainty in estimating the true bias remains quite large when this approach must be used - ~30 DN for heater-off times <2 days and ~50 DN for longer heater-off times. This uncertainty is reflected in the Uncertainty Map image extension for calibrated frames produced by the pipeline (see Section 6).

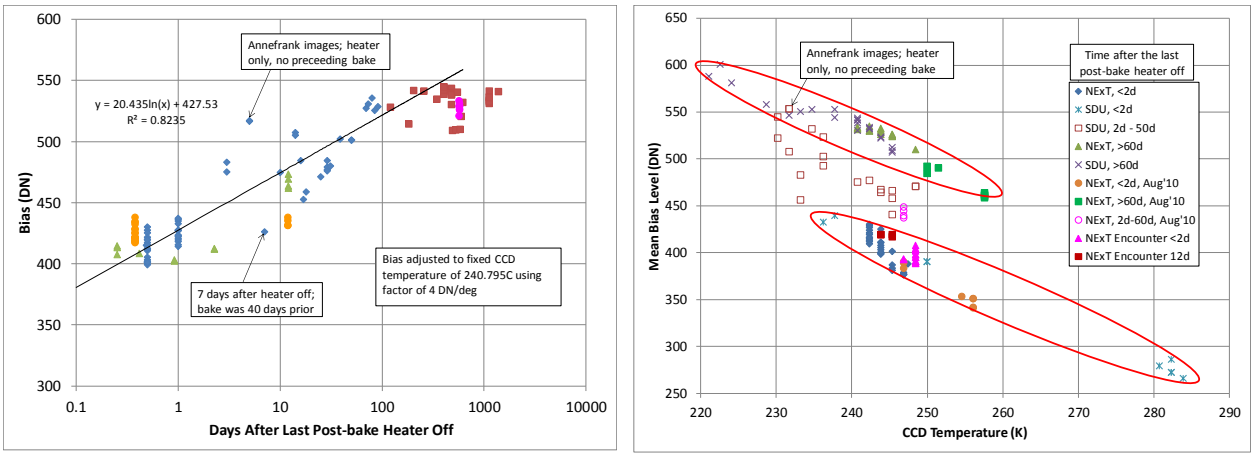

Figure 10 - Dependence of bias level on CCD temperature (right) and time since the CCD heater was turned off (left)

In addition to the bias level, dark current must also be subtracted off as part of proper radiometric calibration. As mentioned in Section 2, NAVCAM does not flush the CCD prior to every integration period; all CCD flushes must be explicitly commanded. Therefore, the dark current builds up from the time of the last CCD readout, which can be 10s to 100s of seconds. So to properly calculate the level of dark current in a frame, both the dark current rate (which is a function of CCD temperature) and the buildup time must be known. In determining the NAVCAM dark current generation rate for a zero-exposure frame, we assume that the signal difference between the active array signal and the bias level in columns 1044-1046 represents dark current signal. Figure 11 shows the measured dark current rates vs. CCD temperature for a variety of frames collected during the prime mission and NExT. The dark current rate is ~0.1 DN/s at typical CCD temperatures. In the pipeline, we use the ground-based calibration rate curve for data acquired prior to 2010 and the inflight rate curve from NExT for data acquired in 2010 and beyond. Note that for both estimated windowed bias and dark current level calculations, supplemental command history files are required to determine CCD heater-off time and the time between CCD frame flushes, since this information is not available in the raw image headers. The information is, however, inserted into the calibrated frame headers.

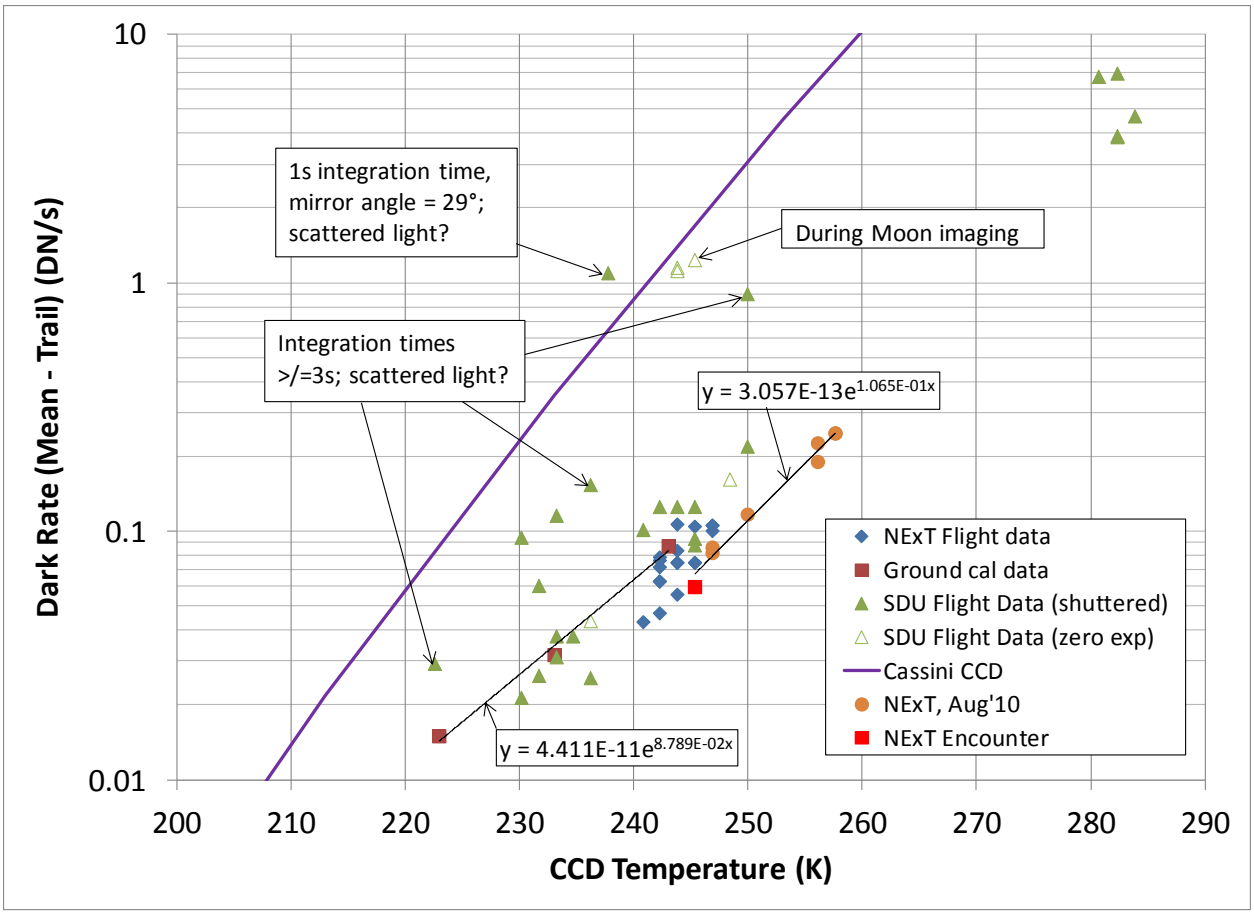

Figure 11 - NAVCAM dark current rate vs. CCD temperature

Absolute radiometric response rate

The absolute radiometric response rate of the NAVCAM (i.e., DN/s for a given scene radiance) was determined from its response while imaging several photometric standard stars (Canopus, bet Hyi, Achernar, Vega, and 16CygA & B; Morel and Magnenat, 1978; Pickles, 1998; Burnashev, 1985). The theoretical basis for this type of calibration is discussed in Klaasen, et al., 2008. We measured the total star signals vs. exposure times, including best-fit shutter offsets. The primary errors in the measurements are due to uncertainties in the correct background level to subtract because: a) most data used windowed frames for which overclocked bias values are not available; b) bias drifts with CCD temperature, the CCD temperature increases with camera operating time, and the telemetered CCD temperature is only quantized in 1.53°C steps; c) many frames contain scattered light spatial gradients across the array; and d) the inherent background noise (~3.4 DN, 1σ) leaves residual errors in computing its mean value.

Aperture photometry was performed on the stars imaged in December 2008 using 17x17 and 51x51-pixel box sizes. The background level was determined from the boundary pixels between 48x48 and 51x51-pixel boxes. The NAVCAM model psf was used to determine the fraction of the total star signal we would expect to capture in each box size, and the measured signal was scaled up by dividing by this fraction to get the best estimate of the total star signal. Based on these measurements, the NAVCAM spectral response math model was adjusted so that the total star signals predicted by the model best matched those measured. Based on the results of the December 2008 calibration, and using the inflight derived gain factor of 25 e-/DN, we found that the measured star signals averaged about 0.93 of the levels predicted by the math model using pre-launch component calibration data. The model CCD quantum efficiency was reduced by this factor to improve the model fits. Figure 12 plots the updated NAVCAM response rate vs. wavelength when observing a flat diffuse reflector of 100% reflectivity at all wavelengths illuminated by the Sun from a distance of 1 AU This updated NAVCAM spectral response model was used to compute the following radiometric calibration factors to scene reflectance (I/F, where I=scene radiance and F=solar irradiance/π) and radiance:

3.89×10^{-5} (I/F units)/(DN/ms) for a solar-illuminated surface at 1 AU
1.93×10^{-9} (W/cm^2/nm/sr)/(DN/ms) for a spectrally flat source radiance.

The system effective wavelength determined this way is 647 nm for I/F measurements (solar spectrum; see http://rredc.nrel.gov/solar/spectra/am0/ for ASTM E490 solar spectrum) and 666 nm for radiance measurements (flat spectrum). Residual scatter of about 10% remains in the actual vs. modeled star signals. This level of uncertainty is what can be expected from the measurement of total signal from a single well-exposed star image. No systematic variations in response rate were observed with position in the FOV.

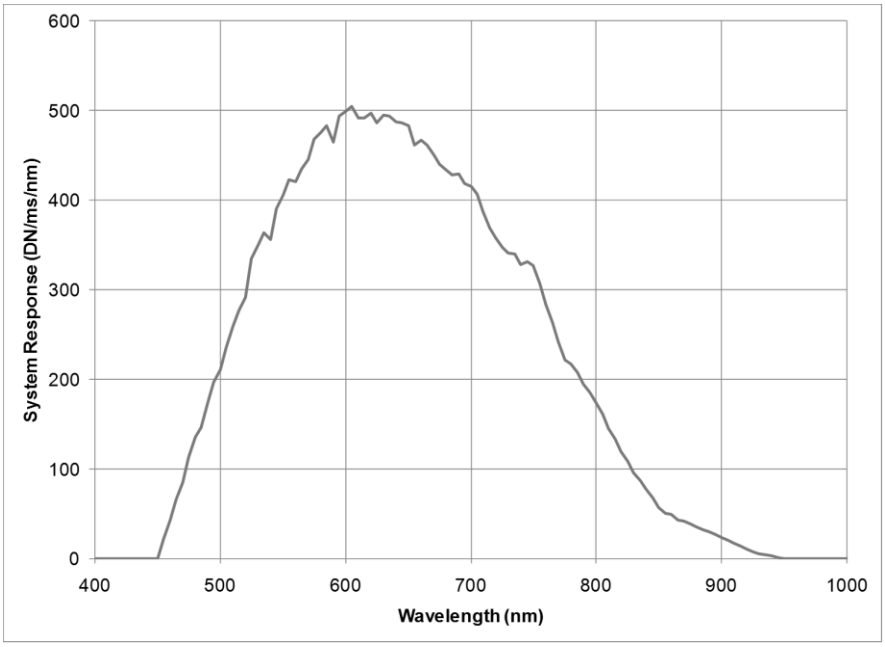

Figure 12 - Modeled NAVCAM spectral response rate to a solar-illuminated surface with I/F=1 at 1 AU based on December 2008 inflight calibration

A similar analysis was done using the star images from the pre- and post-encounter calibrations in 2011. These data exhibited a larger amount of scatter – about 20% after excluding outliers due to low SNR and high scattered light. Contrary to the 2008 results, the 2011 calibrations showed an apparent correlation between signal rate and location of the star in the camera FOV. Lower signal rates were seen for stars imaged near the center of the frame, as illustrated in Figure 13 (left). One possible cause for this change could be residual contamination that is no longer being removed by the bake process. We elected to do a normalization of the data to scale all the measurements to their equivalent value if they had been made at the center of the FOV. Figure 13 (right) shows the best-fit derived normalization function. Applying this normalization reduced the scatter to ~5% for a given aperture box size on a given day.

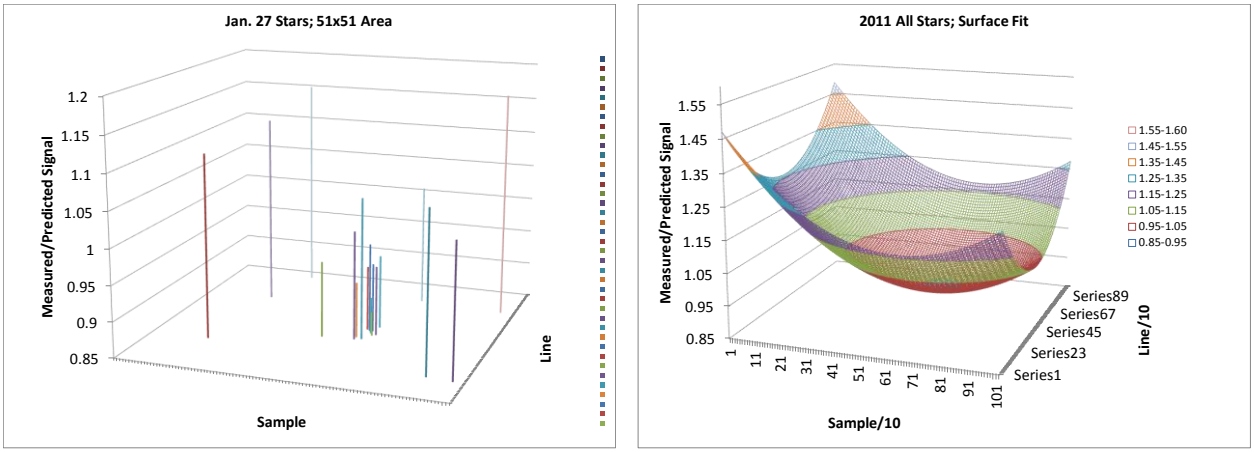

Figure 13 - Measured/predicted star signals across the FOV for the pre-encounter calibration (left) and the best-fit normalization function to adjust all measurements to their equivalent value had they been made at the center of the FOV (right)

Using the average normalized star signals for the two photometry box sizes, the final ratios of the measured star signals to those predicted using the 2008 NAVCAM response model were 0.99 for the pre-encounter calibration and 0.935 for the post-encounter calibration. For calibration of the encounter data beginning on 2/14/11, we choose to adjust the calibration constants in the pipeline by the average of these two values yielding:

4.05×10^{-5} (I/F units)/(DN/ms) for a solar-illuminated surface at 1 AU
2.01×10^{-9} (W/cm^2/nm/sr)/(DN/ms) for a spectrally flat source radiance.

These constants really apply only at the center of the FOV; they may slightly overestimate the scene reflectance or radiance at FOV locations away from the center.

The calibration constants derived above do not include the effects of viewing through the periscope. NAVCAM views entirely or partially through the periscope for scan mirror angles between 0° and 16°. The periscope reduces the light throughput to the NAVCAM, and it produces double images when viewing partially through the periscope (>7° mirror angle). The optical throughput of the periscope was characterized using Stardust images of the Pleiades and Spica and NExT images of the Moon. Figure 14 shows the relative throughput of the periscope vs. scan mirror angle for these images; note that the throughput is slightly different as a function of image line number for a given mirror angle. Images at lower line numbers have their throughput profiles shifted toward higher mirror angles relative to those of images at higher line numbers. The images of Star 1 were located at line numbers ranging between 423 and 526, those for Star 2 ranged between 529 and 638, those for Star 3 ranged between 622 and 749, those for Star 4 ranged between 614 and 715, those for Star 5 ranged between 657 and 790, and those for star 6 ranged between 699 and 812. No throughput dependence on the image sample location was observed over the range of sample numbers from 292 to 598. The Stardust Moon images were located at line numbers ranging between 396 and 488; thus, the fact that the throughput ratios for the Moon fall closest to those of Pleiades Star 1 is consistent with their similar line locations.

The throughput vs. mirror angle plot suggests that as the mirror angle moves away from 0° some additional light starts to be lost when the angle reaches about 5°. Perhaps the periscope no longer fills the scan mirror entrance aperture at this angle. The amount of light lost continues to increase up to a mirror angle of about 9°. Beyond that angle some light that bypasses the periscope starts to be captured by the scan mirror causing the "throughput" to increase. The "throughput" continues to increase with mirror angle as more and more bypass light is captured, until the periscope is no longer in the scan mirror FOV at all at an angle of about 16°.

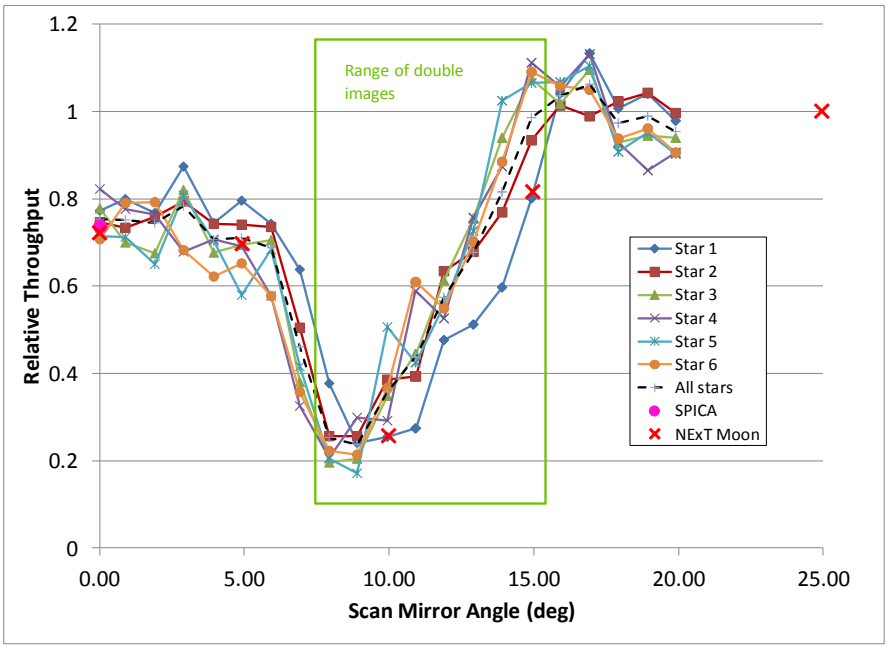

Figure 14 - Relative throughput of the periscope vs. scan mirror angle; six Pleiades stars are numbered in order of increasing line number

The green box in Figure 14 shows the range of scan mirror angles over which double images can occur due to the scan mirror intercepting some light passing through the periscope and some light passing just outside the periscope and forming slightly offset images from each of these ray bundles. Figure 15 (left) plots the fraction of the total star signal contained in each of the doubled images when they occur, and Figure 15 (right) shows the pixel separation between the doubled images. Again, both of these parameters depend on both the mirror angle and the line location of the images. Figure 16 shows a NExT doubled image of the Moon at a scan mirror angle of 15°. No pipeline corrections for reduced periscope throughput or doubled images are currently being implemented.

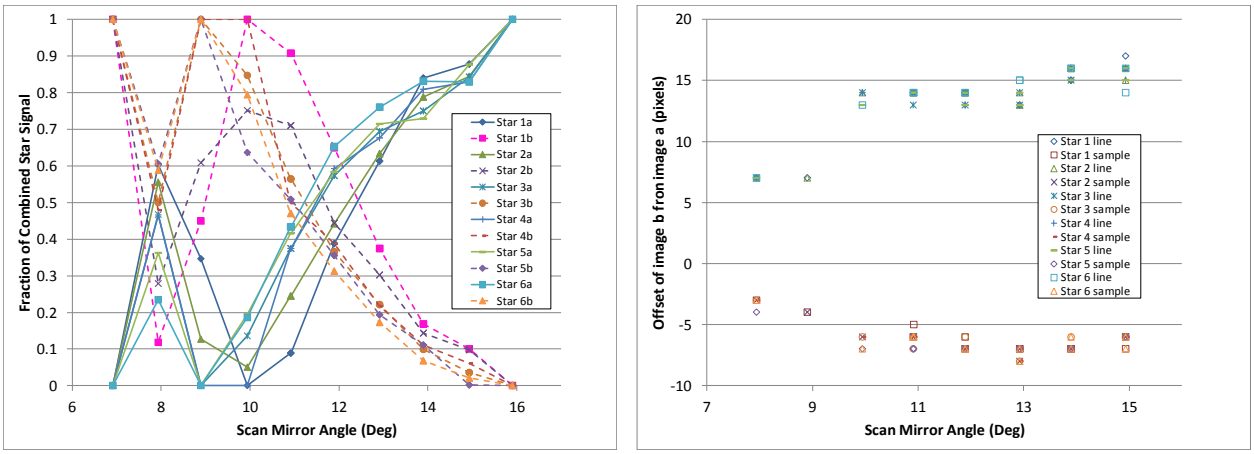

Figure 15 - Signal split and image separation vs. scan mirror angle and line number for doubled images viewed partially through the periscope; light for "a" images bypasses the periscope, light for "b" images passes through the periscope

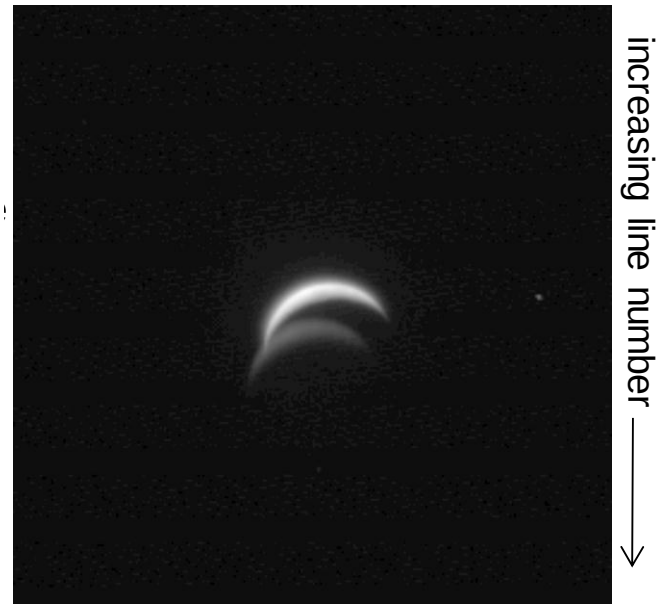

Figure 16 - Doubled image of the Moon taken partially through the periscope at scan mirror angle of 15°; log stretch

Flat field

A NAVCAM flat-field calibration was done pre-launch using integrating sphere images (without the scan mirror; Newburn, et al., 2003a). As can be seen in Figure 17, the optics produce vignetting at the corners of the FOV. Columns 11 and 1034 are "hot columns" having charge levels far higher than those in the rest of the array. These columns produce deferred charge in

the columns immediately to their right (columns 12 and 1035) at levels of 2 – 3% of the charge level in the hot column. No correction for this deferred charge is made in the pipeline.

Figure 17 - NAVCAM pre-launch flat field image using an integrating sphere light source; stretched from 0.781 to 1.056 of the mean value

Inflight flat-field calibration options are minimal. Possible approaches are: a) ratioed cal lamp images (inflight/pre-launch times pre-launch flat), b) image stars at various locations in the FOV (per Figure 13), or c) perhaps using diffuse scattered light input. Residual contamination probably affects the inflight flat-field response, but exactly how is difficult to determine.

We used inflight cal lamp images to monitor the post-bake contamination state. Figure 18 shows a comparison of cal lamp images taken before launch and in flight and the changes that occurred during the NExT mission. As can be seen, the residual contamination after baking was rather minimal and restricted to a few small clumps by December 2008. But after the August 2010 bake, the residual contamination pattern changed significantly, growing in size and number of areas affected. The majority of the residual contamination is located near the center of the FOV. By 14 days after the August 2010 bake, the contamination pattern had become more diffuse, presumably due to the more volatile contamination starting to re-accumulate. The pattern after the post-encounter bake is quite similar to that after the August 2010 bake. The residual contamination pattern during 2011 tends to be somewhat consistent with the spatial distribution of the measured/predicted signal ratios in the calibration star images (Figure 13) and might be its cause (but it may not be the only, or even the primary, cause; spatial variations in response may be due to some other effect that is less patchy, as suggested by the systematic variations seen in

Figure 13). We note, however, that whatever residual contamination there may be, NAVCAM star images remained sharp in all inflight calibrations, and no degradation in spatial resolution is indicated.

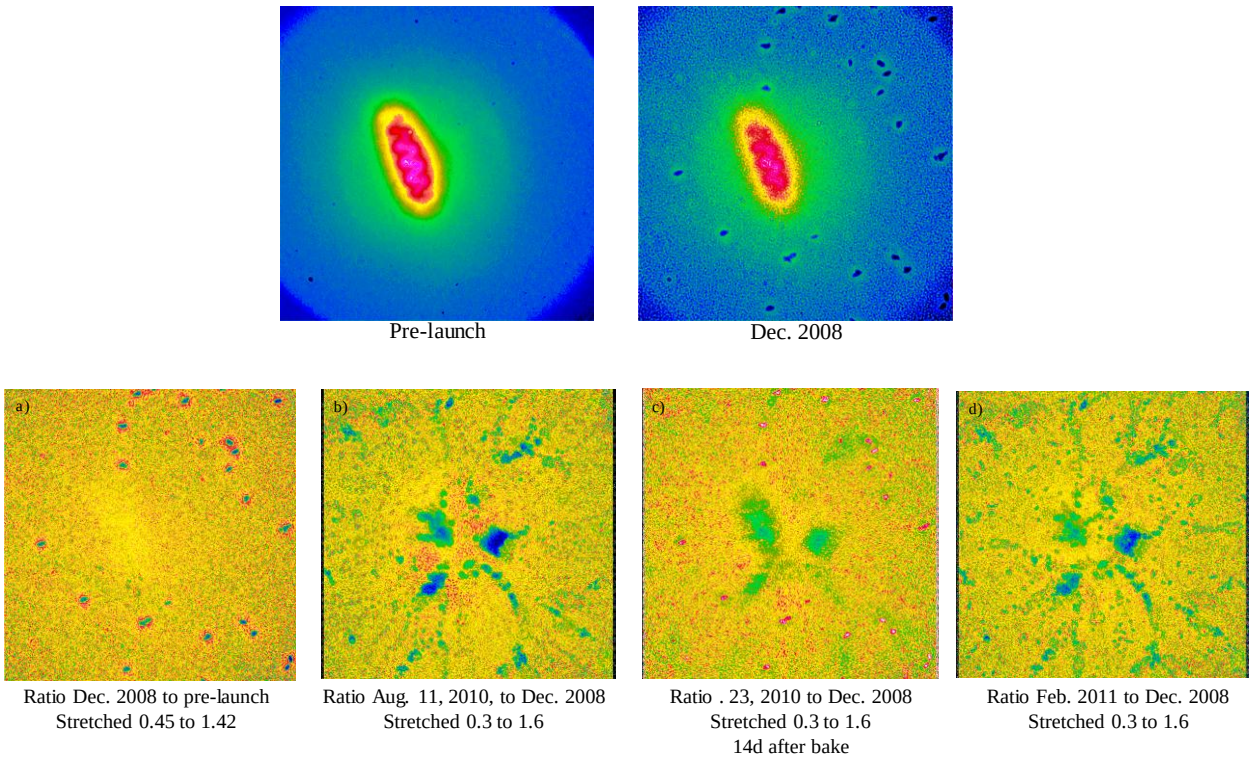

Figure 18 - NAVCAM decontaminated calibration lamp images and ratios showing the accumulation of residual contamination even after baking. DN levels are pseudo-color coded for easier visibility here and in subsequent figures; the color code has black for the minimum, white for the maximum, with intermediate values increasing from blue to red as the wavelength of the color increases.

We must be careful not to assume that the contamination patterns seen in Figure 18 are directly applicable as flat-field corrections for data taken of external targets. The lighting geometry on the CCD from the calibration lamp is different than that from focused external targets. We can see some examples of this in the illumination patterns of scattered light entering the camera from external sources. Figure 19 shows examples of such images taken during the Tempel 1 approach and departure sequences (no long-exposure full frames were taken during these periods, only windowed frames). While the contrast pattern seen in the calibration lamp images of Figure 18 is recognizable, it is not identical, and the pattern moves around within the FOV somewhat (see especially frame n10190te01, a 16CygA+B image taken during the Jan. 27 calibration activity). These variations make a true flat-field correction based on calibration lamp and/or scattered light images very challenging.

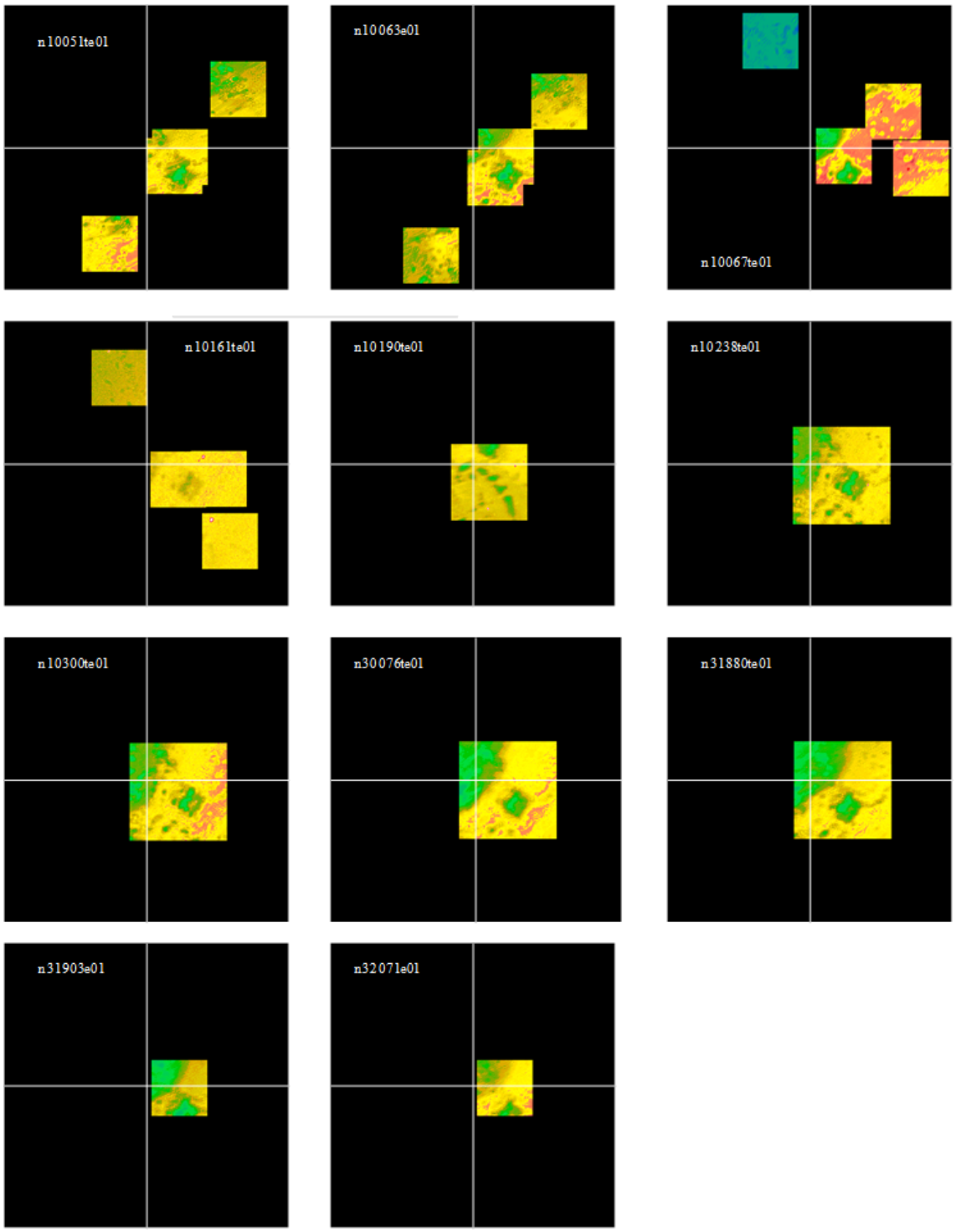

Figure 19 – Examples of contrast caused by residual contamination illuminated by external scattered light from different geometries; returned windows are shown inserted in the proper locations within the FOV

Given the difficulties and instabilities in determining the NAVCAM flat-field response in flight, we have elected to correct only using the pre-launch flat-field calibration file. Cal lamp and scattered light illumination geometries are not the same as for a focused external source. Attempting to correct for the changing residual contamination is too uncertain and could do more harm than good. The star-based paraboloid adjustment discussed above might help, but this would need to be justified by additional science testing before incorporating such a correction into the pipeline. (Note: researchers who may wish to try applying the paraboloid model fit derived in this work to see if it makes their analysis more believable may use this equation for the best-fit paraboloid:

$$z = 7.48e\text{-}7(x\text{-}512)^2\text{-}2.144e\text{-}3(x\text{-}512)+8.70e\text{-}7(y\text{-}512)^2\text{-}2.059e\text{-}5(y\text{-}512)+0.962,$$

where x = sample number and y = line number.) As yet, no evidence of non-uniform response across the FOV of encounter images has been observed or reported.

Scattered light

No light scattering internal to the NAVCAM was detected at more than 0.5 DN/s in 2-s exposures of Canopus (110 saturated pixels; see Figure 22). However, NAVCAM has proved highly susceptible to scattered Sunlight reflected off various spacecraft structures. Significant scattered light has been detected even for Sun-illumination directions at which the NAVCAM was thought to be well shadowed. No comprehensive calibration of scattered light rates vs. Sun direction and mirror angle has been possible; such a calibration would require a huge effort with $>10^6$ frames returned to Earth. However, a sense of the dependence of scattered light levels on the illumination and mirror angle geometries has been provided by accumulated inflight experience.

Figure 20 shows a model of the Stardust spacecraft including its coordinate system and the NAVCAM and periscope mounting locations. The spacecraft is normally positioned at an attitude with the Sun in the +Z hemisphere, most typically in the XZ plane and close to the +Z axis direction. The figure includes a sketch showing the azimuth and elevation convention used here to define the Sun-illumination direction. Figure 20 also shows the scattered light rates measured for frames taken at various Sun-illumination directions and scan mirror angles during both the prime Stardust and NExT missions. In general, we see that scattered light is greatest for mirror angles <30° or >160° or for Sun elevation angles <40°. However, rates in excess of 10 DN/s are also seen for mirror angles >90° and Sun elevation angles as high as 78° when the Sun is in the –X hemisphere.

We included a special scattered light calibration in the December 2008 cruise calibration in which we placed the spacecraft in the same attitude with respect to the Sun direction that it would be for the Tempel 1 encounter and observed with mirror angles of 2°, 7°, 12°, 17°, 22°, 171°, and 176°. These observations are shown as blue filled diamonds in the lower-right plot of

Figure 20. The attitude chosen was for the spacecraft flying with its Whipple shields forward, as expected for encounter. These measurements showed that scattered light would be acceptably small for the encounter. However, we later decided to start the Tempel 1 approach observations with the spacecraft flying backward, i.e., with its Whipple shields in the opposite direction from the velocity vector. This attitude was adopted because it simplified operations, minimized spacecraft attitude maneuvering, and minimized propellant usage. We neglected to appreciate that we had never done a scattered light calibration in that attitude. Unfortunately, in this attitude as the mirror angles increased to 168° and beyond, the scattered light rates increased dramatically (red crosses in lower-right plot of Figure 20). In addition, on departure from Tempel 1 flying forward, the Sun-illumination direction was different enough from our calibration attitude that scattered light again proved much higher than expected for mirror angles above 168°. The scattered light caused substantial degradation in the quality of the approach and departure imagery, which were taken with exposure times of 5, 10 or 20 s. And our experience demonstrated that even small differences in spacecraft attitude and/or mirror angle could cause large changes in the scattered light level.

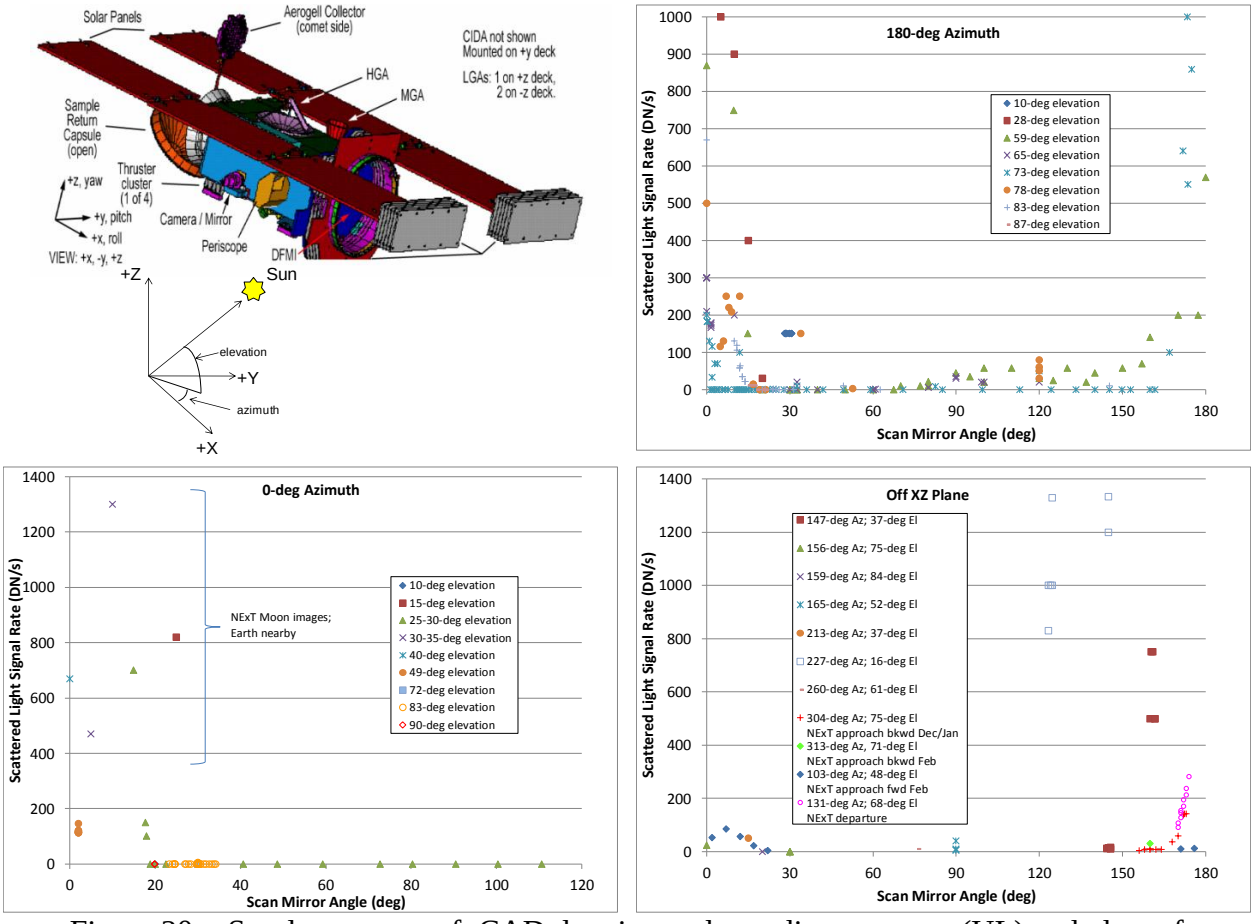

Figure 20 - Stardust spacecraft CAD drawing and coordinate system (UL) and plots of NAVCAM scattered light rates observed for different Sun-illumination and scan mirror angle geometries

A few special cases of elevated scattered light in peculiar ghost image patterns have been observed in frames taken through the periscope. Figure 21 shows the three cases noted to date. The scattered light signal rates are extremely high, >10000 DN/s in the left and center Moon images and ~800 DN/s in the right image, which did not view any specific target. These ghost image patterns are apparently due to internal NAVCAM or periscope reflections. Spots are seen in the ghosts that look like the residual contamination spots in cal lamp images, and there are structures suggestive of secondary mirror spider supports. The ghost signal rates are at about 5% of the maximum Moon signal rate in the Moon frames; however, the lit Earth was within 15° of the Moon, so the ghost could be an Earth illumination effect.

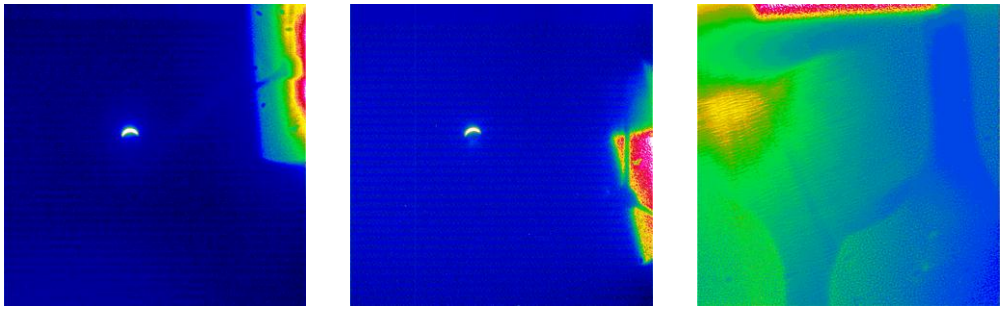

Figure 21 - Ghost reflections observed in a few NAVCAM frames taken through the periscope

Finally, elevated signal levels were observed in dark frames taken while pointed at the Moon. We attribute this to a light leak in the NAVCAM system that allows light at about the 10^{-6} level to reach the detector even when the shutter is closed.

Charge bleeding and residual

As is the case for many CCD detectors, charge generated in excess of a pixel's full-well capacity will bleed up and down the CCD column. We characterized this effect using saturated images of Canopus (see Figure 22). From analysis of such images, we find that the pixel well capacity is about 250,000 e^- (equivalent to ~10000 DN). No bleeding is seen in star, cal lamp, or Moon frames with charge levels up to ~200,000 e^-/pixel. In these saturated Canopus frames, we also observe deferred charge in the first column to the right of a saturated column at a level of ~150 DN. Apparently, the serial register has a lower full-well limit than the active array pixels or contains a small charge trap. The former explanation seems more plausible since we see no deferred charge in any unsaturated star images. In addition, the pixels immediately above and below the saturated portions of a bled column may contain the last of the excess charge, which would elevate their signal levels but not above the 4095 DN encoding limit.

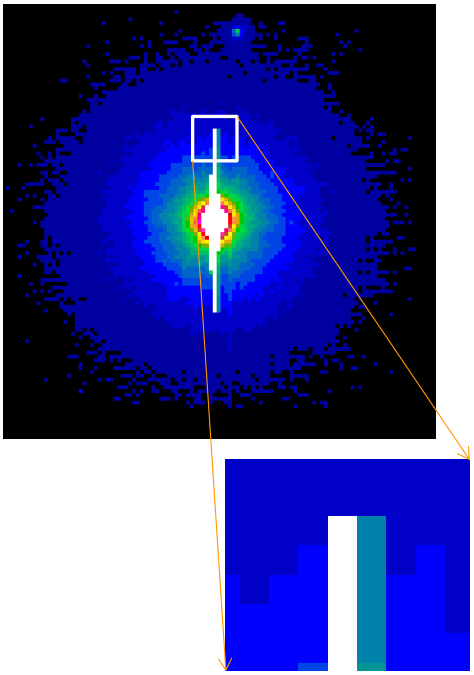

Figure 22 - Charge bleeding along columns from a saturated Canopus image and deferred charge seen in the column to the right

Tests for any sign of residual image charge were conducted using saturated star and Moon frames followed immediately by a dark frame. No evidence of any residual image was seen. A check for evidence of transient quantum efficiency effects from pixel saturation (sometimes called "residual bulk image") was also done using successive partially overlapping Moon images, the first of which was saturated and second of which was not. No sign of distorted isophotes was observed in the second frame indicating that the quantum efficiency was not affected by prior saturation of the pixels.

6. Calibration Pipeline Logic Flow and Data Archiving

To produce calibrated archival data records for NAVCAM, the NExT science team relies on a processing system evolved from that used on the Deep Impact and EPOXI missions and located at Cornell University (Klaasen, et al., 2008). This processing pipeline systematically carries out the normal calibration steps using the best available calibration files and constants. As part of the calibration process, auxiliary data extensions recording the quality of the calibrated value, an estimate of the uncertainty, and the SNR for each pixel are generated in image format and appended to each calibrated image record. The calibration pipeline logic flow is illustrated in Figure 23.

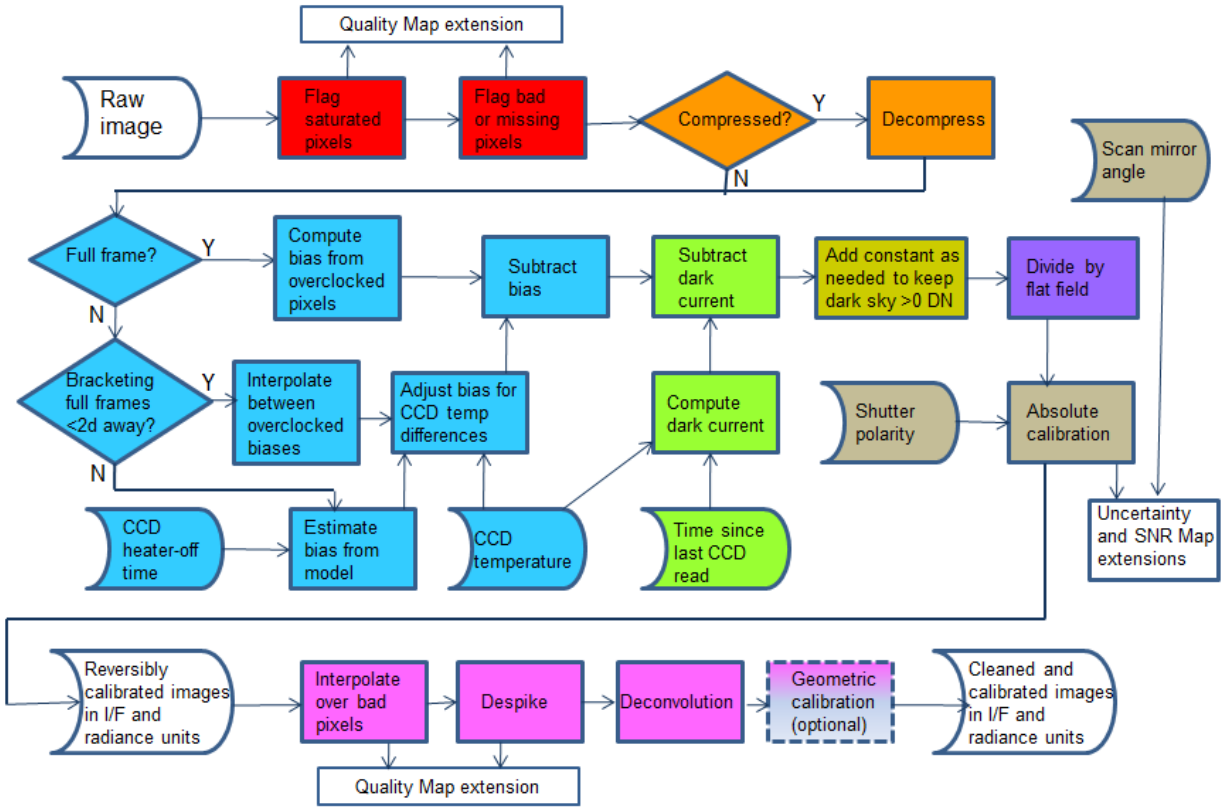

Figure 23 - NAVCAM calibration data processing pipeline logic flow; related functions are grouped by different shading colors

All saturated, bad, or missing pixels are flagged in the quality map extension. Compressed frames are decompressed by reversing the lookup table used to compress the data onboard. The best-estimate bias level and dark current are then subtracted from the image. For images that contain substantial amounts of dark sky, an adjustment is done if necessary to ensure that the bias and dark subtractions have not removed too much signal making dark sky levels go negative. Next the image is divided by the flat field calibration file to correct for variable responsivity across the detector. The data are then converted to absolute radiance and reflectivity units using the radiometric calibration conversion factors and the shutter time (adjusted for shutter offset) and are saved for archiving. The uncertainty and SNR map extensions are generated and stored after this step. Next a series of irreversible adjustments are made to clean up artifacts and improve spatial resolution in the images. Data values in known bad pixel locations are interpolated over from neighboring pixel values. Noise spikes exceeding a specified threshold are also removed via near-neighbor interpolation. These adjustments are recorded in the quality map extension. Spatial resolution is then improved using a deconvolution process with a filter based on the NAVCAM psf. These cleaned up calibrated versions are also saved for archiving. Any geometric calibration is left as a separate option for users to perform if they choose.

The calibration quality map is a byte image map defining the integrity of every pixel. Each bit in the byte for each pixel is set to 1 if a given criterion is met. These flags are:

Bit	Criterion for setting to 1
0	Pixel is outside the commanded returned window(s)
1	Known bad pixel (none have been identified to date)
2	Missing data; data not received from the spacecraft
3	Saturated value
4	Value potentially corrupted by neighboring saturated pixel
5	Interpolated; pixel value reclaimed by interpolating from neighbors
6	Despiked; pixel value modified by the despiking routine
7	Spare

For example, if a pixel is bad and has been reclaimed by interpolation, the decimal value in the quality map will be $2^1+2^5=34$. In the normal FITS format for the calibrated image, this map exists as the first image extension.

The uncertainty map is the next image extension. It provides a percentage uncertainty in the calibrated pixel value (exclusive of random noise). This uncertainty includes the errors due to incorrect estimations of bias level, dark current level, and exposure time and the effects of viewing through the periscope.

The SNR map is as defined for Deep Impact in Klaasen, et al., (2008) with the appropriate NAVCAM values for read noise and gain substituted. This map exists as the last image map extension.

The raw and calibrated data, along with calibration files and other ancillary information, will be archived with the Planetary Data System Small Bodies Node by the fall of 2011 (Veverka, et al., 2011b; Veverka, et al., 2011c).

Conclusion

Significant improvements in the calibration of the Stardust-NExT NAVCAM have been realized through the acquisition of new calibration data during the NExT mission as well as reanalysis of prime mission data. The camera psf was characterized down to an unprecedented level of nearly 10^{-6} of the total point-source star signal. Star images were used to monitor the effectiveness of CCD heating in removing recurring contamination from the detector. Shutter performance was calibrated as a function of image line number and shutter blade movement direction to an accuracy of <0.1 ms. Models for estimating the bias and dark current levels as functions of CCD temperature and time since the CCD heater was last powered off were developed that allow reasonably accurate radiometric calibration of windowed images, which do not return the overclocked pixel values that explicitly provide the bias level. Absolute radiometric response

calibration conversion constants were derived from images of photometric standard stars. Residual contamination patterns were tracked to assess their impact on flat-field calibrations. The dependence of scattered light levels on Sun-illumination and scan mirror position was determined for many geometries. The data processing pipeline has been updated to incorporate these improved calibrations and will be used to generate archival NAVCAM data records for both the NExT (new) and the primary Stardust mission (upgrade), which will be delivered to the Planetary Data System.

Acknowledgements

The work described herein was supported by the National Aeronautics and Space Administration through Contract No. NNM08AA26C from the Discovery Program to Cornell University and through Task Order No. NMO711001 from the Discovery Program to the Jet Propulsion Laboratory, California Institute of Technology.

References

Brownlee, D. E., et al., "The Surface of young Jupiter family comet Wild 2: View from the Stardust spacecraft," *Science*, v. 304, no. 5678, pp. 1764-1769, June 18, 2004.

Burnashev, V. I., "Stellar spectrophotometric catalogue," *Abastumanskaya Astrofiz. Obs. Bull*. 59, 83, 1985.

Duxbury, T. C., et al., "The Asteroid 5535 Annefrank size, shape, and orientation: Stardust first results," *JGR-Planets*, v. 109, issue E2, article E02002, Feb. 6, 2004.

Hillier, J. K., J. M. Bauer, and B. J. Buratti, "Photometric modeling of Asteroid 5535 Annefrank from Stardust observations," *Icarus*, v. 211, pp. 546-552, 2011.

Hog, E., et al., "Construction and verification of the Tycho-2 catalogue," *Astron. Astrophys.*, 357, 367, 2000.

Janesick, J., K. Klaasen, and T. Elliott, "Charge-coupled device charge-collection efficiency and the photon-transfer technique, *Opt. Eng.*, 26, 10, 972, 1987.

Klaasen, K.. P., et al., "Deep Impact instrument calibration," *Review of Scientific Instruments*, 79, 091301, 2008.

Li, J-Y, M. F. A'Hearn, T. L. Farnham, and L. A. McFadden, "Photometric analysis of the nucleus of Comet 81P/Wild 2 from Stardust images," *Icarus*, v. 204, pp. 209-226, 2009.

Morel, M. and P. Magnenat, "UBVRIJKLMNH photoelectric photometric catalog," *Astron. Astropys. Suppl*., 34, 477, 1978.

Newburn, R. L., "Calibration of the STARDUST navigation camera," http://pdssbn.astro.umd.edu/holdings/sdu-c-navcam-3-rdr-wild2-v2.0/document/calrpt/calibrpt.pdf, 2000.

Newburn, R. L., S. Bhaskaran, T. Duxbury, G. Fraschetti, T. Radey, and M. Schwochert, "Stardust imaging camera," *JGR*, v. 108, no. E10, pg. 8116, 2003a.

Newburn, R. L., et al., "Phase curve and albedo of asteroid 5535 Annefrank," *JGR*, v. 108, no. E11, pg. 5117, 2003b.

Pickles, A. J., "A stellar spectral flux library: 1150-25000 Å," *Publications of the Astronomical Society of the Pacific*, 110:863-878, 1998.

Tsou, P., et al., "Stardust encounters comet 81P/Wild 2," *JGR*, v. 109, E12S01, 2004.

Veverka, J., et al., "Return to Comet Tempel 1 : Overview of Results from Stardust-NExT," *Icarus*, this issue, 2011a.

Veverka, J. F., K.P. Klaasen, B.V. Semenov, S.A. McLauglin, B.T. Carcich, and S.E. Sackett, "Stardust-NExT NAVCAM images of 9P/Tempel 1," SDU-C/CAL-NAVCAM-2-NEXT-TEMPEL1-V1.0, NASA Planetary Data System, 2011b.

Veverka, J. F., K.P. Klaasen, B.V. Semenov, S.A. McLauglin, B.T. Carcich, and S.E. Sackett, "Stardust-NExT NAVCAM calibrated images of 9P/TEMPEL 1," SDU-C/CAL-NAVCAM-3-NEXT-TEMPEL1-V1.0, NASA Planetary Data System, 2011c.